ELSEVIER

International Journal of Solids and Structures 41 (2004) 1395–1410

INTERNATIONAL JOURNAL OF SOLIDS and STRUCTURES

www.elsevier.com/locate/ijsolstr

Three-dimensional stress analysis of textile composites. Part II: Asymptotic analysis

Sangwook Sihn [a,*], Endel V. Iarve [a], Ajit K. Roy [b]

[a] *Nonmetallic Division, University of Dayton Research Institute, 300 College Park, Dayton, OH 45469-0168, USA*
[b] *Air Force Research Laboratory, Materials and Manufacturing Directorate, AFRL/MLBC, 2941 P St Rm. 136, WPAFB, OH 45433-7750, USA*

Received 5 June 2003; received in revised form 22 September 2003

Abstract

An asymptotic singular stress analysis was performed in the unit-cell of the plain–woven composite in the vicinity of the yarn–yarn–matrix interface intersection with and without the inter-yarn delamination. The problem was reduced to a three-material wedge singularity type by introducing several curvilinear coordinate systems and systematic expansions in power series of the distance from the contour of the stress singularity.

The power of stress singularity at the inter-yarn and yarn–matrix interface junction was investigated as a function of crimp angle and matrix-to-yarn stiffness ratio. In the case of perfect bonding between the yarns and the matrix with small crimp angles near 9°, the power of singularity is weak (∼0.02) and insensitive to the stiffness ratio of the axial yarn to the matrix material. For increased crimp angles, however, small variations in the stiffness of the matrix material can significantly affect the power of singularity. In the case of the inter-yarn delamination, two singular roots—one crack type (∼0.5) and one weak (∼0.01)—were obtained for all crimp angles and delamination opening modes.

Coefficients of the asymptotic expansion were obtained by comparing the full-field three-dimensional numerical solution based on B-spline displacement approximation method with multi-term asymptotic expansions in the vicinity of the singular point. Good agreement between the two solutions was observed in all examples considered.

Keywords: Woven composites; Asymptotic singular analysis; Inter-yarn stresses

1. Introduction

As concluded in part I, an adjoining paper by Sihn et al. (accepted for publication), the inter-yarn normal and shear stress components in the representative unit-cell model of the woven composites exhibited singular behavior at the three-material junction. The directional nonuniqueness of the stress values in the vicinity of the singular point was discussed by Iarve and Pagano (2001) and cannot be captured by using the

* Corresponding author. Tel.: +1-937-255-9324; fax: +1-937-258-8075.
E-mail address: sangwook@stanfordalumni.org (S. Sihn).

0020-7683/$ - see front matter © 2003 Elsevier Ltd. All rights reserved.
doi:10.1016/j.ijsolstr.2003.11.024

polynomial displacement approximation functions. Therefore, it is essential to incorporate analysis methods, such as asymptotic singular stress analysis, which will be discussed below.

The asymptotic analysis has been performed for free-edge problems in laminated composites to obtain accurate interlaminar stresses at the interface. Wang and Choi (1982) constructed an infinite series elasticity solution for a composite wedge near the ply interface and the wedge edge based on Lekhnitskii's complex variable stress function. The pioneering work by Wang and Choi (1982) was extended by Folias (1992) and Wang and Lu (1993) to carry out an asymptotic solution for interlaminar stresses at the interface around an open-hole edge of a composite plate. They showed that the singular stress solution at the ply interface around the curvilinear hole edge is equivalent to that for the straight edge, provided that a ply orientation with respect to the direction tangential to the hole edge remains the same as the ply orientation in the straight edge with respect to the edge direction. The power of stress singularity was found to be dependent upon the location at the edge of the hole.

Iarve (1996) developed a B-spline-based approximation method for three-dimensional (3-D) stress solution of laminated composites with the open hole. The numerically calculated stress solution near the hole edge using this method was compared with one given by the singular term from the asymptotic solution. At the singularity, the polynomial spline approximation did not capture directional nonuniqueness of singular stress functions. However, it was observed that the singular term of the asymptotic solution with appropriate coefficient and constant additive terms matched the full-field spline solution to a distance of approximately one-half ply thickness from the singular point. The large area of agreement suggested a hybrid method by superposing the singular term with the polynomial approximation to determine the stress field more efficiently and reliably without extreme mesh refinement near the free-edge stress singularity. The asymptotic solution in combination with the B-spline-based numerical solution of the singular stress field at the intersection of the ply interface with a through-thickness hole was developed by Iarve (1997, 2000) and Iarve and Pagano (2001) for 3-D analysis for the open-hole and pin-loaded joints.

The present work extends the asymptotic analysis to the singular stress problems arising in textile composites. The analysis will be performed at and near the interface region of the three material junction with yarns and matrix. The asymptotic solution will be compared with the numerical full-field solution based on the B-spline approximation method.

2. Asymptotic analysis

Singular stress distribution at the triple material connection will be investigated by using the asymptotic analysis. The analysis will focus on the three inter-yarn boundaries between the bottom matrix (subregions 5), the warp yarn (subregions 1) and the fill yarn (subregions 2), as shown with a rectangle in Fig. 1(a).

The singular points at the triple material connection are located on a contour, Γ_1, in Fig. 1(b), which can be described in the following parametric form,

$$x = L_w/2, \quad y = c_1(s), \quad z = c_2(s) \quad \text{for } 0 \leqslant s \leqslant L_f. \tag{1}$$

The two functions, $c_1(s)$ and $c_2(s)$ can be written by using Eq. (1) in part I as

$$c_1(s) = s, \quad c_2(s) = t_f + t_w\left(1 - \cos\frac{\pi s}{L_f}\right) \quad \text{for } 0 \leqslant s \leqslant L_f. \tag{2}$$

An orthogonal curvilinear coordinate system, *rst*, whose origin slides along the contour, Γ_1, and *rt*-plane is normal to the tangential direction of the contour Γ_1, shown in Fig. 1(b), was introduced as follows:

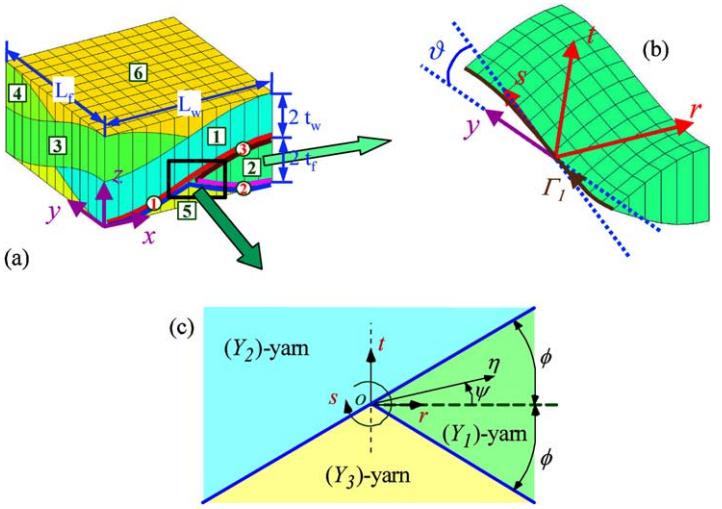

Fig. 1. A representative unit-cell of plain–woven composites, geometric parameters and global and local coordinate systems for asymptotic analysis. Numbers in boxes are subregion numbers, and numbers in circles are interface numbers.

$$\begin{cases} x = r + L_w/2, \\ y = c_1(s) - t\sin\vartheta, \\ z = c_2(s) + t\cos\vartheta, \end{cases} \tag{3}$$

where ϑ is a crimp angle of the fill yarn between the y- and s-axes on the yz-plane, as shown in Fig. 1(b), which can be expressed as

$$\cos\vartheta = \frac{c_1'(s)}{\sqrt{(c_1'(s))^2 + (c_2'(s))^2}}, \quad \sin\vartheta = \frac{c_2'(s)}{\sqrt{(c_1'(s))^2 + (c_2'(s))^2}}, \tag{4}$$

where $c' = \mathrm{d}c/\mathrm{d}s$.

With unit vectors ($\mathbf{e}_r$, $\mathbf{e}_s$ and $\mathbf{e}_t$) in the curvilinear *rst*-coordinate system, one can write a gradient vector as

$$\nabla = \mathbf{e}_r\frac{\partial}{\partial r} + \mathbf{e}_s\frac{1}{g_s}\frac{\partial}{\partial s} + \mathbf{e}_t\frac{\partial}{\partial t}. \tag{5}$$

where $g_s = \sqrt{(c_1'(s))^2 + (c_2'(s))^2} - t\frac{\mathrm{d}\vartheta}{\mathrm{d}s}$.

The gradient of an arbitrary displacement vector yields strain components in the *rst*-coordinates as follows:

$$\varepsilon_1 = \varepsilon_{rr} = \frac{\partial u_1}{\partial r},$$

$$\varepsilon_2 = \varepsilon_{ss} = \frac{1}{g_s}\left(\frac{\partial u_2}{\partial s} - u_3\frac{\partial\vartheta}{\partial s}\right),$$

$$\varepsilon_3 = \varepsilon_{tt} = \frac{\partial u_3}{\partial t},$$

$$\varepsilon_4 = 2\varepsilon_{st} = \frac{\partial u_2}{\partial t} + \frac{1}{g_s}\left(\frac{\partial u_3}{\partial s} + u_2\frac{\partial\vartheta}{\partial s}\right),$$

$$\varepsilon_5 = 2\varepsilon_{rt} = \frac{\partial u_1}{\partial t} + \frac{\partial u_3}{\partial r},$$
$$\varepsilon_6 = 2\varepsilon_{rs} = \frac{\partial u_2}{\partial r} + \frac{1}{g_s}\frac{\partial u_1}{\partial s}, \tag{6}$$

where the displacement components (u_i) correspond to u_r, u_s, u_t for $i = 1, \ldots, 3$, correspondingly.

A dot product of the gradient vector and the stress tensor yields equilibrium equations as follows:

$$\frac{\partial \sigma_1}{\partial r} + \frac{1}{g_s}\left(\frac{\partial \sigma_6}{\partial s} - \sigma_5 \frac{\partial \vartheta}{\partial s}\right) + \frac{\partial \sigma_5}{\partial t} = 0,$$
$$\frac{\partial \sigma_6}{\partial r} + \frac{1}{g_s}\left(\frac{\partial \sigma_2}{\partial s} - 2\sigma_4 \frac{\partial \vartheta}{\partial s}\right) + \frac{\partial \sigma_4}{\partial t} = 0, \tag{7}$$
$$\frac{\partial \sigma_5}{\partial r} + \frac{1}{g_s}\left(\frac{\partial \sigma_4}{\partial s} + \sigma_2 \frac{\partial \vartheta}{\partial s} - \sigma_3 \frac{\partial \vartheta}{\partial s}\right) + \frac{\partial \sigma_3}{\partial t} = 0,$$

where the stress components (σ_i) correspond to σ_{rr}, σ_{ss}, σ_{tt}, σ_{st}, σ_{rt}, σ_{rs} for $i = 1, \ldots, 6$, correspondingly.

The constitutive relations in the *rst* coordinates are expressed in the contracted notation as

$$\sigma_i = Q_{ij}\varepsilon_j, \tag{8}$$

where Q_{ij} are stiffness coefficients in *rst*-coordinates, whose matrix form can be written as

$$[Q]_{rst} = [T_2(-\vartheta)]^{\text{fill}}[C]_{\text{global}}\left([T_2(-\vartheta)]^{\text{fill}}\right)^T, \tag{9}$$

where $[T_2(-\vartheta)]^{\text{fill}}$ is the transformation matrix of the fill yarn in Eq. (15) in part I.

Next, we introduce $\eta\psi$-coordinates in the *rt*-plane according to the following expression:

$$r = L_w \cdot \eta\cos\psi, \quad t = L_w \cdot \eta\sin\psi, \tag{10}$$

where $\eta \geqslant 0$ and $0 \leqslant \psi \leqslant 2\pi$, as shown in Fig. 1(c). The $\eta\psi s$-coordinates, which are commonly used for the asymptotic stress analysis, allow us to express the stress-strain components in Eqs. (6) and (7) as functions of distance from the singular contour Γ_1.

One can write derivatives of an arbitrary function F with respect to the *rst*-coordinates as

$$\frac{\partial F}{\partial r} = \Lambda_t F \quad \text{and} \quad \frac{\partial F}{\partial t} = \Lambda_n F, \tag{11}$$

where

$$\Lambda_t F = \cos\psi\frac{\partial F}{\partial \eta} - \frac{\sin\psi}{\eta}\frac{\partial F}{\partial \psi}, \quad \Lambda_n F = \sin\psi\frac{\partial F}{\partial \eta} + \frac{\cos\psi}{\eta}\frac{\partial F}{\partial \psi}. \tag{12}$$

These expressions allow us to estimate the order of $\partial/\partial r$ and $\partial/\partial t$ terms in Eqs. (6) and (7). If $\eta \to 0$, all terms in Eq. (11) are of the order $O(F/\eta)$. Therefore, $\partial u_i/\partial r$, $\partial u_i/\partial t$, $\partial \sigma_i/\partial r$ and $\partial \sigma_i/\partial t$ terms in Eqs. (6) and (7) are of the order $O(u_i/\eta)$ and $O(\sigma_i/\eta)$, respectively. To evaluate the order of terms with the *s*-direction derivatives, one can write

$$g_s = \sqrt{(c_1'(s))^2 + (c_2'(s))^2} - \eta\sin\psi\frac{\mathrm{d}\vartheta}{\mathrm{d}s}. \tag{13}$$

When the contour of singularity is smooth and has no kinks, there will be a positive number R such that $\sqrt{(c_1'(s))^2 + (c_2'(s))^2} > R$, where R would have the meaning of a minimum value of curvature on the singular contour. Therefore, if $\eta \to 0$, g_s remains finite, and thus the terms $\partial u_i/\partial s$ and $\partial \sigma_i/\partial s$ in Eqs. (6) and (7) are of the order $O(u_i)$ and $O(\sigma_i)$, respectively, which become small as compared with $\partial/\partial r$ and $\partial/\partial t$ related terms.

By using Eqs. (6)–(8) and (11) and maintaining only the dominant singular terms, Navier equations of equilibrium for a given yarn/matrix can be written as

$$(\Lambda_t \mathbf{A} \Lambda_t + \Lambda_n \mathbf{B} \Lambda_t + \Lambda_n \mathbf{C} \Lambda_n) \begin{Bmatrix} u_1 \\ u_2 \\ u_3 \end{Bmatrix} = 0, \tag{14}$$

where the symmetric square (3×3) matrices, **A**, **B**, **C**, are expressed as follows:

$$\mathbf{A} = \begin{bmatrix} Q_{11} & Q_{16} & Q_{15} \\ & Q_{66} & Q_{56} \\ \text{symm} & & Q_{55} \end{bmatrix}^{(Y_i)}, \quad \mathbf{B} = \begin{bmatrix} 2Q_{15} & Q_{14}+Q_{56} & Q_{13}+Q_{55} \\ & 2Q_{46} & Q_{36}+Q_{45} \\ \text{symm} & & 2Q_{35} \end{bmatrix}^{(Y_i)} \quad \text{and}$$

$$\mathbf{C} = \begin{bmatrix} Q_{55} & Q_{45} & Q_{35} \\ & Q_{44} & Q_{34} \\ \text{symm} & & Q_{33} \end{bmatrix}^{(Y_i)}, \tag{15}$$

and the superscript (Y_i) indicated the (i)th yarn as shown in Fig. 1(c). It was assumed that the derivatives of the stiffness coefficients Q_{ij} in $\partial/\partial r$, $\partial/\partial s$, $\partial/\partial t$ were of the order $O(\eta)$, and, therefore, became negligible as $\eta \to 0$.

A homogeneous solution of the displacement field of the Navier equations in Eq. (14) can be obtained in the following formula (Iarve, 1996):

$$u_i^{(Y_j)} = \eta^{\lambda} \sum_{k=1}^{6} f_k^{(Y_j)} \left(\sin\psi + \mu_k^{(Y_j)} \cos\psi \right)^{\lambda} d_{ki}^{(Y_j)}, \quad i = 1,2,3, \tag{16}$$

where $\mu_k^{(Y_j)}$ and $d_{ki}^{(Y_j)}$, which are given in Appendix A, are eigenvalues and eigenvectors obtained by solving sixth-order polynomial characteristic equations for each yarn (Y_j), and $f_k^{(Y_j)}$ and λ are arbitrary complex constants to be determined from the inter-yarn boundary conditions.

From Eqs. (6), (8) and (16), one can obtain the stress components as follows:

$$\begin{aligned} \sigma_i &= \lambda \eta^{\lambda-1} \sum_{k=1}^{6} f_k (\sin\psi + \mu_k \cos\psi)^{\lambda-1} [\mu_k (Q_{i1} d_{k1} + Q_{i6} d_{k2}) + Q_{i3} d_{k3}], \quad i = 1,2,3,6, \\ \sigma_i &= \lambda \eta^{\lambda-1} \sum_{k=1}^{6} f_k (\sin\psi + \mu_k \cos\psi)^{\lambda-1} [Q_{i5} d_{k1} + Q_{i4} d_{k2} + \mu_k Q_{i5} d_{k3}], \quad i = 4,5. \end{aligned} \tag{17}$$

The power λ and the coefficients f_k are to be determined from the boundary conditions at the interface between yarns and matrix. We considered two types of inter-yarn boundary conditions corresponding to undamaged and partially delaminated inter-yarn surfaces. For undamaged inter-yarn surfaces, displacement and traction continuity conditions are applied at the yarn interfaces. In the rt-plane, the interfaces between yarns (Y_1 and Y_2), (Y_2 and Y_3) and (Y_1 and Y_3) correspond to $\psi = \phi$, $\psi = \pi + \phi$ and $\psi = -\phi$, respectively, as shown in Fig. 1(c).

To apply the inter-yarn boundary conditions, $\{u\}_{rst}$ and $\{\sigma\}_{rst}$ vectors were rotated by using the transformation matrices $[L_2(\phi)]^{\text{warp}}$ and $[T_2(\phi)]^{\text{warp}}$ of the warp yarn in Eqs. (11) and (14) in part I, such that

$$\{u\}_{\eta\psi s} = [L_2(\phi)]^{\text{warp}} \{u\}_{rst}, \tag{18}$$

$$\{\sigma\}_{\eta\psi s} = [T_2(\phi)]^{\text{warp}} \{\sigma\}_{rst}. \tag{19}$$

Then the desired boundary conditions can be expressed as

$$\begin{cases} u_i^{(Y_1)} = u_i^{(Y_2)} & \text{at } \psi = \phi, \\ u_i^{(Y_2)} = u_i^{(Y_3)} & \text{at } \psi = \pi + \phi, \\ u_i^{(Y_3)} = u_i^{(Y_1)} & \text{at } \psi = -\phi, \end{cases} \quad i = \eta, \psi, s, \tag{20}$$

$$\begin{cases} \sigma_i^{(Y_1)} = \sigma_i^{(Y_2)} & \text{at } \psi = \phi, \\ \sigma_i^{(Y_2)} = \sigma_i^{(Y_3)} & \text{at } \psi = \pi + \phi, \\ \sigma_i^{(Y_3)} = \sigma_i^{(Y_1)} & \text{at } \psi = -\phi, \end{cases} \quad i = \psi\psi, \eta\psi, s\psi. \tag{21}$$

Refer to Appendix A for solution details. The full-field stresses in the finite volume around the singular contour can then be represented as

$$\sigma_i = \sum_{j=1}^{\infty} K_j(\vartheta)\eta^{\lambda_j - 1}\bar{\sigma}_i(\lambda_j, \psi) + \mathrm{O}(\eta^{\lambda_1}), \quad i = 1, \ldots, 6, \tag{22}$$

where $\bar{\sigma}_i(\lambda, \psi)$, which was introduced for brevity, can be obtained by comparing Eq. (22) with Eq. (17). To define coefficients of the asymptotic expansion, $K_j(\vartheta)$, $\bar{\sigma}_i(\lambda, \psi)$ was normalized by $\bar{\sigma}_3(\lambda, \phi)$.

The presence of $\mathrm{O}(\eta^{\lambda_1})$ terms in Eq. (22), where λ_1 is the smallest eigenvalue obtained from Eq. (14), is due to the fact that only the dominant singular terms were taken into account in Eq. (14). By doing so, we omitted a series of roots with $\mathrm{Re}[\lambda] > \mathrm{Re}[\lambda_1] + 1$, where λ_1 is the dominant singular term. As pointed out by Iarve (1996), the analytical treatment of these secondary roots in the general case of orthotropic materials has not been presented in the literature. However it appeared that the influence of such terms can be accurately captured by using numerical solutions.

3. Results

The asymptotic analysis was performed near the singular point at $x = L_w/2$, $y = 0$ and $z = t_f/2$ in Fig. 1(a), where interface lines 1–3 intersect in the unit-cell of the plain–woven composite. Fig. 1(c) shows the region of the asymptotic analysis surrounding the singular points where the fill yarn (Y_1), warp yarn (Y_2) and matrix materials (Y_3) join. The yarn crimp angle at the singular point is $\phi = \tan^{-1}(\pi t_w/L_w) = 8.927°$.

The characteristic values (μ_k) in Eq. (A.1) were ± 0.7190i, ± 1.3908i, $\pm$i for the fill yarn, ± 0.2045i, ± 1.5151i, $\pm$i for the warp yarn, and ± 0.9996i, ± 1.0004i, $\pm$i for the matrix material. Only one root of $\lambda_1 = 0.9781$ was found within $0 < \mathrm{Re}(\lambda) < 1$ from the asymptotic analysis. This singular root corresponds to the power of singularity of $1 - \lambda = 0.0219$, which provides weak singularity compared to a crack singularity of 0.5. The smallest nonsingular, noninteger roots found within $\mathrm{Re}(\lambda) > 1$ were $\lambda_2 = 1.0714$, $\lambda_3 = 1.9445$ and $\lambda_4 = 2.0347$, etc.

Under certain loading conditions causing a large deformation of the yarns in the unit-cell of the plain–woven composites, the yarn crimp angle may not be preserved at $\phi = 8.927°$. In this case, it is necessary to know how the stress singularity behaves with the change of the crimp angles. A parametric study was performed by varying the yarn crimp angle (ϕ) from 0° to 45°. Both noninteger singular and nonsingular roots were calculated within $0 < \mathrm{Re}(\lambda) < 2$. Distributions of these roots against the crimp angle are plotted in Fig. 2. All the roots were pure real numbers. The singular root (λ_1) decreased monotonically as the crimp angle increased, but still created weak singularity of $(1 - \lambda) < 0.1$. One of the nonsingular roots (λ_2) monotonically increased with the angle increase, while the other root (λ_3) had a maximum approximately at $\phi = 15°$.

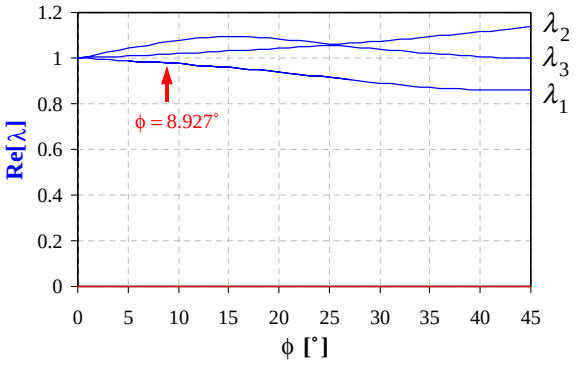

Fig. 2. Distributions of singular and nonsingular roots from asymptotic analysis against yarn crimp angles.

The material properties of yarn and matrix in the woven fabric composites can have variation because of the variability in fabrication methods and processing conditions. For example, a resin transfer molding (RTM) process with fiber preforms can create a resin-rich area or voids in the matrix regions. Even though most of the applied loadings are carried by the longitudinal warp and transverse fill yarns, stress field change with the property variation of the matrix material is also of interest. Another parametric study was performed by varying the Young's modulus of the matrix (E_m) from a hypothetically large value of longitudinal Young's modulus of yarn (E_1) to zero for a resin-free void. In this case, only the singular root was calculated with two crimp angles of $\phi = 8.927°$ and 30°. Distributions of the roots as functions of E_m/E_1 ratio were plotted in Fig. 3. Note that $E_m/E_1 = 0.027$ for $E_m = 3.75$ GPa. The singular roots at the hypothetical $E_m/E_1 = 1$ were 0.72 and 0.70 at $\phi = 8.927°$ and 30°, which yielded relatively high singularities of $(1 - \lambda) = 0.28$ and 0.3, respectively. The singular root increased monotonically as the E_m/E_1 ratio decreased. It is interesting to see that the singularity disappeared gradually as the ratio E_m/E_1 approached approximately 0.06 ($E_m = 8.03$ GPa) for both crimp angles. As the material ratio decreased further, the root values decreased again, increasing the power of singularity. Note that the zero matrix material properties simulated a composite notch problem without the matrix region. When the crimp angle is small at $\phi = 8.927°$, the decrease was not significant. However, with the crimp angle of $\phi = 30°$, the root decreased rapidly as the ratio decreased so that the power of singularity near the zero material ratio increased to the level of that with the hypothetical ratio of $E_m/E_1 = 1$. Therefore, a small variation of matrix material

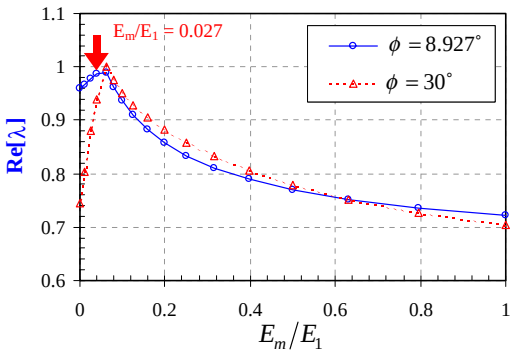

Fig. 3. Distributions of singular roots from asymptotic analysis against ratio of Young's modulus of matrix material to longitudinal modulus of yarns.

properties can significantly affect the power of stress singularity, especially at large crimp angles, which can be developed under large deformation.

When the woven composites are damaged so that one or more yarns are disconnected along the interface boundaries, the displacement and stress continuity conditions in Eqs. (20) and (21) need to be modified. Suppose that a delamination formed along the yarn boundary on line 3 in Fig. 1(a). In the crack-opening mode, the boundary conditions at the yarn interfaces can be written as follows:

$$\begin{cases} u_i^{(Y_2)} = u_i^{(Y_3)} & \text{at } \psi = \pi + \phi, \\ u_i^{(Y_3)} = u_i^{(Y_1)} & \text{at } \psi = -\phi, \end{cases} \quad i = \eta, \psi, s, \tag{23}$$

$$\begin{cases} \sigma_i^{(Y_2)} = \sigma_i^{(Y_3)} & \text{at } \psi = \pi + \phi, \\ \sigma_i^{(Y_3)} = \sigma_i^{(Y_1)} & \text{at } \psi = -\phi, \end{cases} \quad i = \psi\psi, \eta\psi, s\psi, \tag{24}$$

$$\sigma_i^{(Y_1)} = \sigma_i^{(Y_2)} = 0 \quad \text{at } \psi = \phi, \quad i = \psi\psi, \eta\psi, s\psi. \tag{25}$$

Along with the displacement and stress continuity conditions on the undamaged interfaces in Eqs. (20) and (21), Eq. (25) prescribes zero interfacial normal and shear stress conditions on the crack surface. A total of 18 equations are still used as in the undamaged case.

The characteristic values (μ_k) in Eq. (A.1) are also the same as those in the undamaged case, since the same materials are used for the yarns and matrix subregions. Singular roots of λ_1, $\lambda_2 = 0.4571 \pm 0.0057\mathrm{i}$ and $\lambda_3 = 0.9879$ were obtained within $0 < \mathrm{Re}(\lambda) < 1$ from the asymptotic analysis. These roots correspond to the power of singularity of $\mathrm{Re}[1 - \lambda] = 0.5429$ and 0.0121, respectively. Note that λ_1 and λ_2 exhibited strong crack-type singularity. The nonsingular roots were also found as $\lambda_4 = 1.3742$, $\lambda_5 = 1.5059$ and $\lambda_6 = 1.9930$ within $1 < \mathrm{Re}(\lambda) < 2$.

Complex roots, λ_1, $\lambda_2 = 0.4571 \pm 0.0057\mathrm{i}$, resulted in complex numbers of the stress amplitudes ($\bar{\sigma}_i$), and of the coefficients of the asymptotic expansion (K_j). Note that the conjugated roots yielded the same distribution of real and imaginary parts of $\bar{\sigma}_i$ and, therefore, only one of the roots was considered in the asymptotic calculation. The asymptotic stress components for a complex root λ_1 in Eq. (22) can be rewritten as

$$\begin{aligned} \sigma_i &= K_1 \eta^{\lambda_1 - 1} \bar{\sigma}_i(\lambda_1, \psi) + \mathrm{O}(\eta^{\lambda_1}), \quad i = 1, \ldots, 6 \\ &= K_1 \eta^{\mathrm{Re}(\lambda_1) - 1} [\{\mathrm{Re}(\bar{\sigma}_i)\cos\omega - \mathrm{Im}(\bar{\sigma}_i)\sin\omega\} + \mathrm{i}\{\mathrm{Re}(\bar{\sigma}_i)\sin\omega + \mathrm{Im}(\bar{\sigma}_i)\cos\omega\}] + \mathrm{O}(\eta^{\lambda_1}), \end{aligned} \tag{26}$$

where $\omega = \mathrm{Im}(\lambda_1)\ln|\eta|$. With the complex number of K_1, Eq. (26) becomes

$$\begin{aligned} \sigma_i = \overline{K}_1 \eta^{\mathrm{Re}(\lambda_1) - 1} \{\mathrm{Re}(\bar{\sigma}_i)\cos\omega - \mathrm{Im}(\bar{\sigma}_i)\sin\omega\} + \overline{K}_2 \eta^{\mathrm{Re}(\lambda_1) - 1} \{\mathrm{Re}(\bar{\sigma}_i)\sin\omega + \mathrm{Im}(\bar{\sigma}_i)\cos\omega\} + \mathrm{O}(\eta^{\lambda_1}), \\ i = 1, \ldots, 6, \end{aligned} \tag{27}$$

where $\overline{K}_1$ and $\overline{K}_2$ are pure real numbers. Therefore, the complex conjugate roots result in two-term asymptotic expansion.

Fig. 4 shows the distributions of the singular roots against the yarn crimp angle (ϕ) varying from 0° to 45°. In this crack-opening case, two strong roots were obtained near 0.5, and were pure real numbers for $9° < \phi < 39°$ and complex conjugates for other angles. Besides, pure real numbers of weak singular roots were distributed near $\lambda \approx 0.99$.

In the case of a closed delamination of the yarn boundary on line 3, the boundary conditions at the yarn interfaces can be written as follows:

$$\begin{cases} u_i^{(Y_2)} = u_i^{(Y_3)} & \text{at } \psi = \pi + \phi, \\ u_i^{(Y_3)} = u_i^{(Y_1)} & \text{at } \psi = -\phi, \end{cases} \quad i = \eta, \psi, s, \tag{28}$$

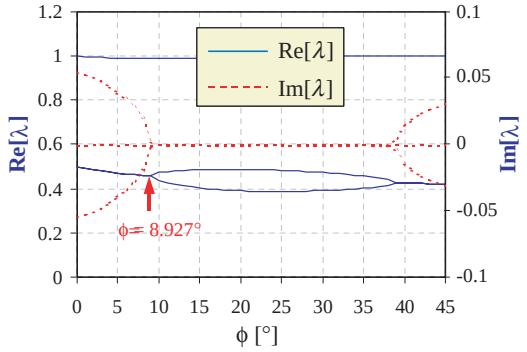

Fig. 4. Distributions of singular roots from asymptotic analysis against yarn crimp angles with crack-opening delamination problem.

$$\begin{cases} \sigma_i^{(Y_2)} = \sigma_i^{(Y_3)} & \text{at } \psi = \pi + \phi, \\ \sigma_i^{(Y_3)} = \sigma_i^{(Y_1)} & \text{at } \psi = -\phi, \end{cases} \quad i = \psi\psi, \eta\psi, s\psi, \tag{29}$$

$$\begin{cases} u_\psi^{(Y_1)} = u_\psi^{(Y_2)}, \\ \sigma_{\psi\psi}^{(Y_1)} = \sigma_{\psi\psi}^{(Y_2)}, \\ \sigma_{\eta\psi}^{(Y_1)} = \sigma_{s\psi}^{(Y_1)} = \sigma_{\eta\psi}^{(Y_2)} = \sigma_{s\psi}^{(Y_2)} = 0. \end{cases} \quad \text{at } \psi = \phi. \tag{30}$$

Eq. (30) prescribes the continuity conditions of the normal displacement and stress as well as the zero interfacial shear stress conditions on the contact surface. The displacement and stress continuity conditions on the undamaged interfaces are the same as in Eqs. (28) and (29), and thus the total number of equations is 18.

With the characteristic values (μ_k), the singular roots were $\lambda_1 = 0.4161$ and $\lambda_2 = 0.9875$ within $0 < \mathrm{Re}(\lambda) < 1$, and the nonsingular roots were $\lambda_3 = 1.0184$, $\lambda_4 = 1.3705$ and $\lambda_5 = 1.9925$ within $1 < \mathrm{Re}(\lambda) < 2$. The singular roots correspond to the power of singularity of $\mathrm{Re}[1 - \lambda] = 0.5839$ and 0.0125, respectively.

Fig. 5 shows the distributions of the singular roots against the yarn crimp angle (ϕ) varying from 0° to 45°. In this closed delamination case, no complex roots were found in the interval $0 < \mathrm{Re}(\lambda) < 2$. The similarity with the open-delamination case is that there are two essential singular roots, one strong ($\lambda \leqslant 0.5$) and one weak ($\lambda \approx 0.99$).

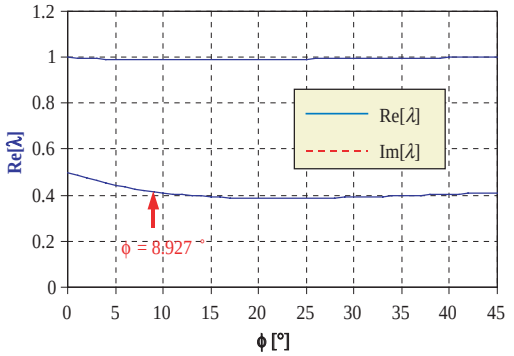

Fig. 5. Distributions of singular roots from asymptotic analysis against yarn crimp angles with crack-closing contact problem.

4. Comparison of asymptotic and full-field numerical calculations

The asymptotic singular stress components were correlated with 3-D B-spline-based numerical solutions obtained in part I, an adjoining paper by Sihn et al. (accepted for publication). Because of the weak nature of the singularity, the comparisons between the asymptotic and the numerical solutions were made with both the singular and the nonsingular roots. The coefficients of the asymptotic expansion (K_j) in Eq. (22) were determined by comparing the stress components from the asymptotic solution with those from the full-field numerical solution for $\eta \ll 1$.

To obtain a more accurate numerical solution with more mesh refinement near the singular point of the present interest, a model woven laminate with one-dimensional yarn crimps was analyzed instead of the plain–woven composites with two-dimensional yarn crimping. The model laminate has the yarn crimping only in the global x-axis but not in the y-axis, as shown in Fig. 6. The cross section at $y = 0$ was the same as that of the plain–woven composites, which resulted in the same dimensions and the same yarn crimp of $\phi = 8.927°$ as those of the plain–woven composites.

The plate was loaded with a constant displacement (u_o) in the x-direction under the following boundary conditions:

$$u_x(0, y, z) = 0, \quad u_x(L_w, y, z) = u_o, \quad u_y(x, 0, z) = u_y(x, L_f, z) = u_z(x, y, 0) = 0. \tag{31}$$

For the undamaged unit-cell of the model woven composites, cubic B-spline functions were used for the displacement approximation in the x-direction with the number of subdivisions in half-length of $n_x = 6$ and in the z-direction with $n_z = 10$, whereas linear functions were used in the y-direction with $n_y = 4$. Non-uniform meshes were used to concentrate the subdivisions to the singular point at $x = L_w/2$, $z = t_f/2$, with the mesh density of $q = 1.5$. For the damaged unit-cell analysis, more refined meshes were used because of the higher stress concentration than for the undamaged one. The quadratic spline functions were used with $n_x = 24$ and $n_z = 48$ in the x- and z-directions, whereas linear functions were used in the y-direction with $n_y = 2$. The mesh density of the nonuniform meshes was $q = 1.2$ toward $X = L_w/2$, $Z = t_f/2$. The stress results were normalized by $\sigma_o = u_o/L_w$ GPa.

The stress results obtained by using the numerical and the asymptotic solution were compared in two different ways:

1. Stress distributions along contours of constant radii with the center at the singular point of $x = L_w/2$, $z = t_f/2$: The stresses were calculated in local $\eta\psi s$-axes with $\psi = \phi$. The radius of the contour was denoted as $\rho = \eta L_w$. The stress distributions were plotted at the radii of $\eta = 0.01$, 0.02 and 0.03 for the undamaged one, and of $\eta = 0.005$, 0.0075 and 0.01 for the damaged ones for a closer look. In both cases, the contour with the smallest radius was used to determine the coefficients of the asymptotic expansion.
2. Stress distributions in local $\eta\psi s$-axes with $\psi = \phi$ along interface lines 1 and 3, and with $\psi = -\phi$ along line 2 in Fig. 1(a). The distance between the interface lines was denoted by a dimensionless parameter, $z^* = (z - t_f)/t_f$. The stress distributions were plotted at the distances of $z^* = \pm 0$. These locations correspond to the interface in the upper and lower yarns, respectively. The comparisons were performed by using the coefficients of the asymptotic expansion obtained from the circular contours.

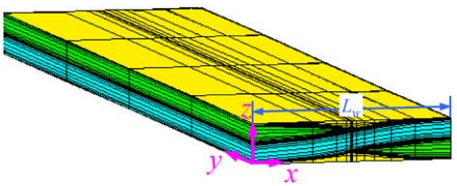

Fig. 6. Model woven laminate composites with one-dimensional yarn crimps.

4.1. Undamaged inter-yarn boundaries

Fig. 7 shows the stress distributions along the contours of constant radii by the asymptotic and the numerical analyses in local $\eta\psi s$-axes with $\psi = \phi = 8.927°$. In this and subsequent figures, the stress components from asymptotic and numerical solutions were plotted with solid and dotted lines, respectively. The comparisons were made with the coefficients of the asymptotic expansion of $K_1 = -0.33$, $K_2 = 0$, $K_3 = -0.72$ and $K_4 = 0.25$ for the roots $\lambda_1 = 0.9781$, $\lambda_2 = 1.0714$, $\lambda_3 = 1.9445$ and $\lambda_4 = 2.0347$, respectively. The shear stress components ($\bar{\sigma}_{\eta s}$ and $\bar{\sigma}_{s\psi}$) in a plane normal to the asymptotic plane are not shown here since they are exactly and approximately zero from the asymptotic and the numerical analyses, respectively. Good agreement was observed between the full-field numerical and asymptotic solutions for all stress components along the three contours. Note that the inter-yarn stress components ($\bar{\sigma}_{\psi\psi}$ and $\bar{\tau}_{\eta\psi}$) are continuous at the yarn interface of $\psi = +\phi$ and $\psi = \pi + \phi$. The displayed agreement indicates that the BSAM numerical calculation yields accurate stress solution near the singular field but requires significant mesh refinement to obtain this accuracy.

Fig. 8 shows the distributions of the interfacial normal ($\sigma_{\psi\psi}$) and shear ($\tau_{\eta\psi}$) stress components along interface lines 1–3 in Fig. 1(a). The same coefficients of the asymptotic expansion were used for the comparisons. Note that the figures were zoomed in toward the singular point within a range of half of the yarn thickness (t_w). As Fig. 8 shows, the stress components provided by the asymptotic solution satisfy the inter-yarn traction continuity precisely. The stress values exhibit infinite growth only in the immediate vicinity of the singularity due to the weakly singular nature of the stress fields. The numerical solution shows traction discontinuity error within $-0.1 < x/t_w < 0.1$ despite the significant mesh refinement. Note that the numerical solution plotted with the rectangular marker on the dotted line in Fig. 8(b) exhibits continuous shear stress distribution along the upper side of interface lines 1 and 3. This continuity contradicts the behavior of the asymptotic solution. Rather, the stress distribution along the lower side having

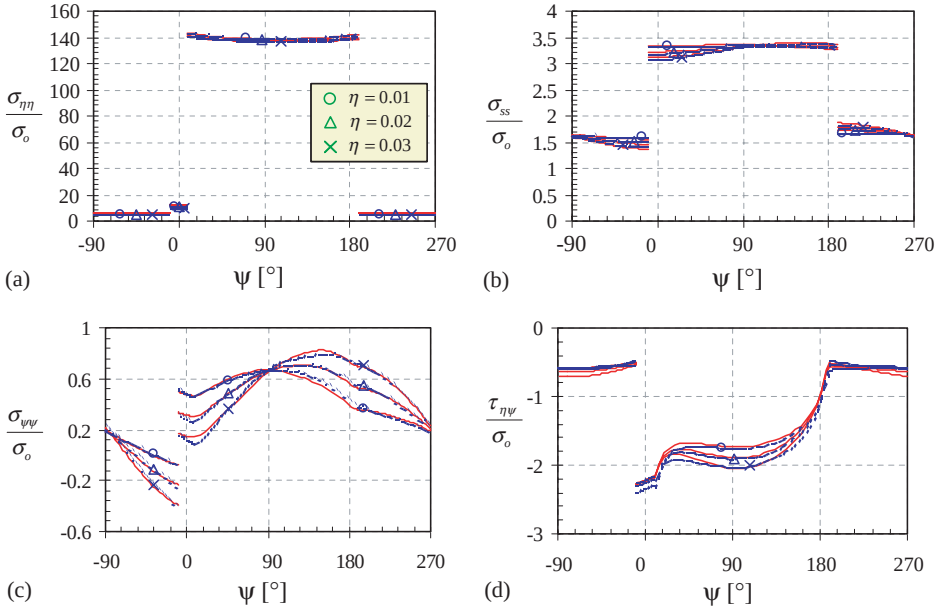

Fig. 7. Stress distribution in local $\eta\psi s$-axes with $\psi = \phi = 8.927°$ along contours of constant radii with the center at the singular point of $x = L_w/2$, $z = t_f/2$. Solid and dotted lines are asymptotic and numerical solutions, respectively. (a) In-plane normal stress ($\sigma_{\eta\eta}$), (b) in-plane normal stress (σ_{ss}), (c) inter-yarn normal stress ($\sigma_{\psi\psi}$) and (d) inter-yarn shear stress ($\tau_{\eta\psi}$).

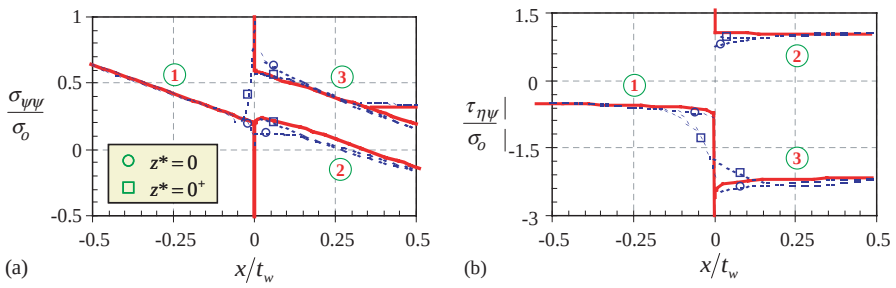

Fig. 8. Stress distribution in local $\eta\psi s$-axes with $\psi = \phi = 8.927°$ along interface lines 1 and 3, and with $\psi = -\phi$ along line 2 in Fig. 1(a): Solid and dotted lines are asymptotic and numerical solutions, respectively. (a) Inter-yarn normal stress ($\sigma_{\psi\psi}$) and (b) inter-yarn shear stress ($\tau_{\eta\psi}$).

the stress jump, which is plotted with the circular marker, is in better agreement with the asymptotic solution. Overall good agreement between the numerical and asymptotic solutions certainly provides confidence in the former. Moreover, an extension of the combined solution procedure (Iarve and Pagano, 2001) to the woven geometry can provide accurate stress field solution without extreme mesh refinement by capturing the singular behavior by the 2-D asymptotic solution.

4.2. Delaminated inter-yarn boundaries

Fig. 9 shows the stress distributions along the contours of constant radii in local $\eta\psi s$-axes with $\psi = \phi = 8.927°$ in the case of the opening delaminated yarns between subregions 1 and 2. While the delamination was modeled as the curved surfaces in the numerical analysis, it was treated as a straight line along the damaged interface at $\psi = 8.927°$ in the asymptotic analysis. The comparisons were made with the coefficients of the asymptotic expansion of $\overline{K}_1 = 2.3$, $\overline{K}_2 = 5$, $K_3 = -1$ and $K_4 = 1$ for the roots $\lambda_1, \lambda_2 = 0.4571 \pm 0.0057\mathrm{i}$, $\lambda_3 = 0.9879$ and $\lambda_4 = 1.3742$, respectively. Good agreement was observed between the full-field numerical solution and the asymptotic one for all stress components along the three contours. Note that the inter-yarn stress components ($\sigma_{\psi\psi}$ and $\tau_{\eta\psi}$) are continuous at the yarn interface of $\psi = +\phi$ and $\psi = \pi + \phi$. Furthermore, these stress components are zero at the yarn interface of $\psi = +\phi$ because of the stress-free condition at the crack surfaces.

Fig. 10 shows the distributions of the interfacial normal ($\sigma_{\psi\psi}$) and shear ($\tau_{\eta\psi}$) stress components along interface lines 1–3 in Fig. 1(a). The same coefficients of the asymptotic expansion were used for the comparisons. As seen from the asymptotic solution, the stress components exhibit a different and rapid growth pattern along interface lines 1 and 2 due to a strong crack-type of singularity, starting at a distance from the singular point significantly farther than the undamaged case, while they are zero along the stress-free interface on line 3. The tractions obtained from the asymptotic solutions from the lower ($z^* = 0^-$) and upper ($z^* = 0^+$) sides coincide exactly with each other. Because of the strong singularity from the crack interface, the numerical solution exhibits more significant errors with highly fluctuating stresses near the singular point despite the significant mesh refinement. Note that the complex value of λ implies oscillating behavior of the exact solution near the singularity. However, the Dundur's parameter appears to be very small (0.0057), so that no such oscillations are visible on the plotting scale of Fig. 10.

Fig. 11 shows the stress distributions along the contours of constant radii in local rst-axes with $\psi = \phi = 8.927°$ in the case of the closed delamination between subregions 1 and 2. The comparisons were made with the coefficients of the asymptotic expansion of $K_1 = 0.14$, $K_2 = 0.2$, $K_3 = -30$ and $K_4 = -0.7$ for the roots $\lambda_1 = 0.4161$, $\lambda_2 = 0.9875$, $\lambda_3 = 1.0184$ and $\lambda_4 = 1.3705$, respectively. Note that high value of K_3 relative to the other K's is due to the small stress amplitude of the K_3 root. The agreement between the full-

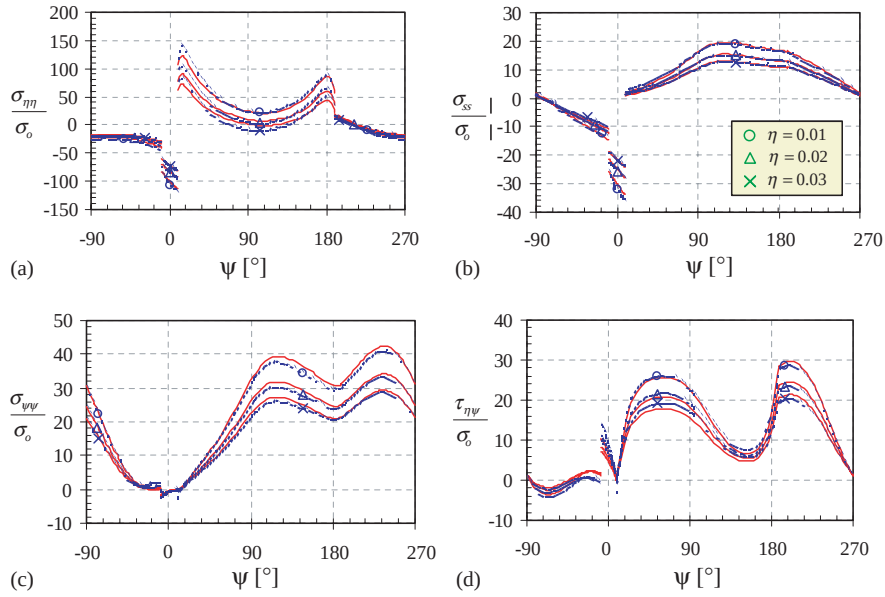

Fig. 9. Stress distribution in local $\eta\psi s$-axes with $\psi = \phi = 8.927°$ along contours of constant radii with the center at the singular point of $x = L_w/2$, $z = t_f/2$. The yarns are delaminated at $\psi = 8.927°$ and loaded in the opening mode. Solid and dotted lines are asymptotic and numerical solutions, respectively. (a) In-plane normal stress ($\sigma_{\eta\eta}$), (b) in-plane normal stress (σ_{ss}), (c) inter-yarn normal stress ($\sigma_{\psi\psi}$) and (d) inter-yarn shear stress ($\tau_{\eta\psi}$).

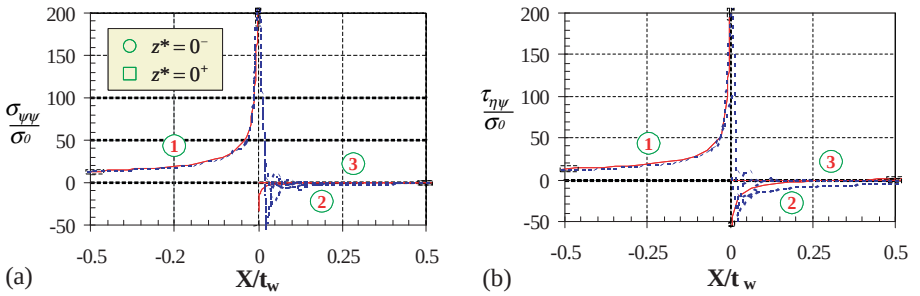

Fig. 10. Stress distribution in local $\eta\psi s$-axes with $\psi = \phi = 8.927°$ along interface lines 1 and 3, and with $\psi = -\phi$ along line 2 in Fig. 1(a). The yarns are delaminated at $\psi = 8.927°$ and loaded in opening mode. Solid and dotted lines are asymptotic and numerical solutions, respectively. (a) Inter-yarn normal stress ($\sigma_{\psi\psi}$) and (b) inter-yarn shear stress ($\tau_{\eta\psi}$).

field numerical solution and the asymptotic one is less precise than the previous cases. However, all stress distributions show unmistakable resemblance. Better agreement can be achieved by incorporating more singular terms in the comparison of the two solutions. Note that the inter-yarn stress components ($\sigma_{\psi\psi}$ and $\tau_{\eta\psi}$) are continuous at the yarn interface of $\psi = +\phi$ and $\psi = \pi + \phi$, and $\tau_{\eta\psi}$ is zero at the yarn interface of $\psi = +\phi$ because of the frictionless contact condition at the contact surfaces.

Fig. 12 shows the distributions of the interfacial normal ($\sigma_{\psi\psi}$) and shear ($\tau_{\eta\psi}$) stress components along interface lines 1–3 in Fig. 1(a). The same coefficients of the asymptotic expansion were used for the comparisons. As seen from the asymptotic solution, the stress components grew infinitely on approaching the singular point along interface lines 1–3, except the zero shear stress component along the frictionless

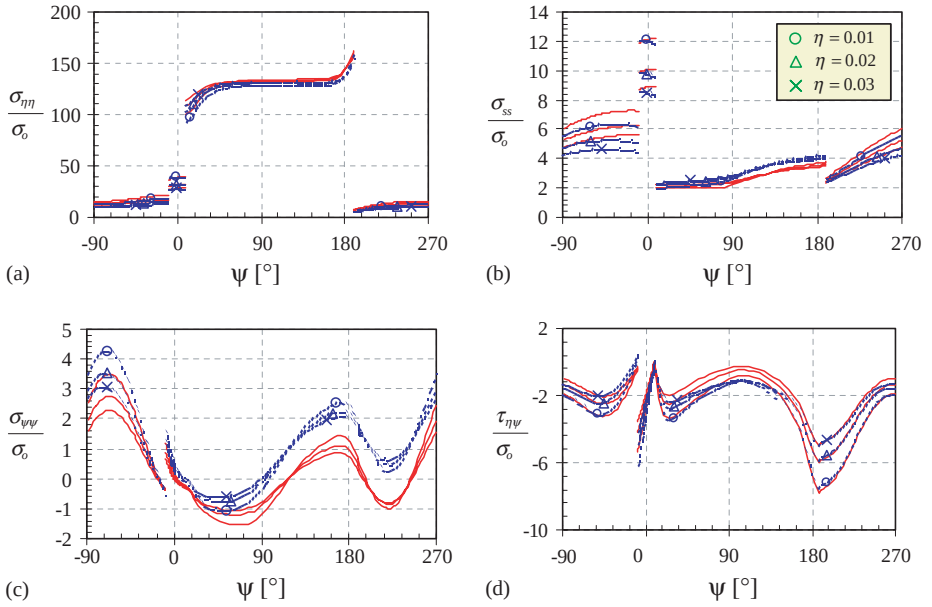

Fig. 11. Stress distribution in local $\eta\psi s$-axes with $\psi = \phi = 8.927°$ along contours of constant radii with the center at the singular point of $x = L_w/2$, $z = t_f/2$. The yarns are delaminated at $\psi = 8.927°$ and loaded in closing mode. Solid and dotted lines are asymptotic and numerical solutions, respectively. (a) In-plane normal stress ($\sigma_{\eta\eta}$), (b) in-plane normal stress (σ_{ss}), (c) inter-yarn normal stress ($\sigma_{\psi\psi}$) and (d) inter-yarn shear stress ($\tau_{\eta\psi}$).

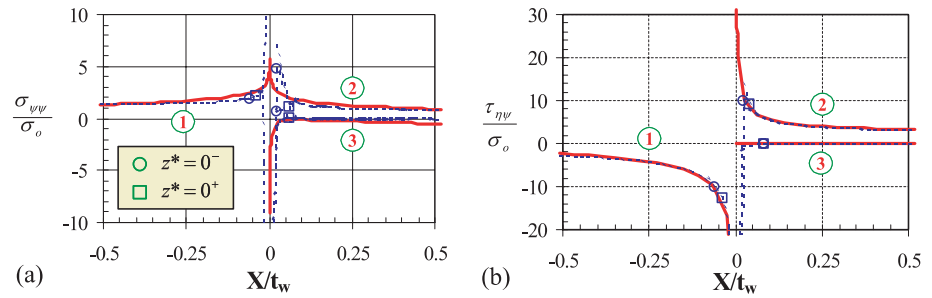

Fig. 12. Stress distribution in local $\eta\psi s$-axes with $\psi = \phi = 8.927°$ along interface lines 1 and 3, and with $\psi = -\phi$ along line 2 in Fig. 1(a). The yarns are delaminated at $\psi = 8.927°$ and loaded in closing mode. Solid and dotted lines are asymptotic and numerical solutions, respectively. (a) Inter-yarn normal stress ($\sigma_{\psi\psi}$) and (b) inter-yarn shear stress ($\tau_{\eta\psi}$).

interface on line 3. Because of the strong singularity from the contact interface, the numerical solution exhibits more significant errors with highly fluctuating stresses near the singular point despite the significant mesh refinement.

5. Summary and conclusions

Asymptotic analysis was performed to obtain a reliable stress field on textile woven composites at the yarn crimp with curvilinear yarns and matrix materials. The analysis was performed at and near the

interface region of the three-material junction with yarns and matrix. Three material interface asymptotic solutions were obtained to describe the stress distributions with and without the inter-yarn delamination.

The power of stress singularity at the inter-yarn and yarn–matrix interface junction was investigated as a function of crimp angle and matrix-to-yarn stiffness ratio. In the case of the perfect bonding between the yarns and the matrix with small crimp angles (for example, near 9°), the power of singularity is weak (~0.02) and insensitive to the stiffness ratio of the axial yarn to the matrix material. For increased crimp angles, however, small variations in the stiffness of the matrix material can significantly affect the power of singularity. In the case of the inter-yarn delamination, two singular roots—one crack type (~0.5) and one weak (~0.01)—were obtained for all crimp angles and both delamination opening and closed modes.

The coefficients of the asymptotic expansion were obtained by comparing the full-field, 3-D numerical solution based on the B-spline displacement approximation method with the multi-term asymptotic expansions in the vicinity of the singular point. For both the undamaged and damaged cases, good agreement was observed for the stress distributions between the two solutions. A combined B-spline numerical and asymptotic solution procedure will be developed to provide an accurate inter-yarn stress field in critical locations with reasonable numerical mesh densities.

Acknowledgement

This work was sponsored by the Air Force Research Laboratory, under contract no. F33615-00-D-5006.

Appendix A

The general solution for Eq. (14) can be found as a superposition of solutions $\{u_1, u_2, u_3\}^T = \omega^\lambda \mathbf{d}$, where $\mathbf{d}$ is an unknown constant complex vector and $\omega = \eta(\sin\psi + \mu\cos\psi)$. Substituting this expression into Eq. (14), one can obtain characteristic eigenvalues, $\mu_k^{(Y_j)}$, from the following sixth-order polynomial characteristic equation,

$$\det|\mathbf{A}\mu_k^2 + \mathbf{B}\mu_k + C| = 0 \tag{A.1}$$

and eigenvectors $d_{ki}^{(Y_j)}$ from the following characteristic matrix,

$$(\mathbf{A}\mu_k^2 + \mathbf{B}\mu_k + \mathbf{C})\begin{Bmatrix} d_{k1} \\ d_{k2} \\ d_{k3} \end{Bmatrix} = 0. \tag{A.2}$$

It will be understood that coefficients μ_k and vectors d_{ki} are constant for each yarn material; therefore the superscript (Y_j) is subsequently omitted, unless needed for clarity.

For orthotropic materials such as the warp and fill yarns, Eq. (A.1) yields six different roots such that $\mu_k = -\mu_{k+3}$, $k = 1, 2, 3$. For isotropic materials such as the matrix material, there are only two different roots, $\pm\sqrt{-1}$ of triple multiplicity. Since the solution in Eq. (16) is valid only if all characteristic roots are distinct, the isotropic material is treated as a slightly orthotropic material by perturbing the elastic properties, E and v with a *coefficient of anisotropy* ($\tau = 10^{-7}$) such that

$$\begin{aligned} &E_1 = (1+\tau)E, \quad E_2 = E_3 = E, \\ &v_{12} = v_{13} = v, \quad v_{23} = (1+10\tau)v, \\ &G_{23} = \frac{E}{2(1+v_{23})}, \quad G_{12} = G_{13} = (1+\tau)G_{23}. \end{aligned} \tag{A.3}$$

By substituting Eqs. (18) and (19) into the boundary conditions in Eqs. (20) and (21), one can obtain a total of 18 equations with 18 unknowns: $f_k^{(Y_1)}$, $f_k^{(Y_2)}$ and $f_k^{(Y_3)}$, $k = 1, \ldots, 6$, such that

$$\mathbf{M} \cdot \mathbf{f} = \mathbf{0}, \quad \mathbf{f} = \left\{ f_1^{(Y_1)}, \ldots, f_6^{(Y_1)}, f_1^{(Y_2)}, \ldots, f_6^{(Y_2)}, f_1^{(Y_3)}, \ldots, f_6^{(Y_3)} \right\}^T, \tag{A.4}$$

where $\mathbf{M}$ is a coefficient matrix of $f_k^{(Y_j)}$. Nontrivial solutions of Eq. (A.4) are obtained by requiring the determinant of the coefficient matrix to be equal to zero, such that $|\mathbf{M}| \equiv g(\lambda) = 0$. The determinant of the system of equations, $g(\lambda) = 0$, is a transcendental equation, which yields an infinite number of roots for the parameter λ. Note that the roots yielding singular stress behavior reside within $0 < \mathrm{Re}(\lambda) < 1$. The roots for the transcendental equation are obtained numerically using a secant method. Two initial guesses of λ were used to obtain the determinants, $g(\lambda_0)$ and $g(\lambda_1)$. A new refined root (λ_2) is then updated by

$$\lambda_2 = \lambda_1 - \frac{g(\lambda_1)(\lambda_1 - \lambda_0)}{g(\lambda_1) - g(\lambda_0)}. \tag{A.5}$$

After substituting the guesses (λ_0 and λ_1) with (λ_1 and λ_2), Eq. (A.5) is recalculated to update λ_2. The procedure repeats until $\lambda_2 \approx \lambda_1$. For a searched root of λ, the coefficients $f_k^{(Y_j)}$ are then obtained. Note that since the coefficients $f_k^{(Y_j)}$ can only be obtained with an arbitrary multiplicative factor, one of the coefficients in $\mathbf{f}$ needs assigned.

References

Folias, E.S., 1992. On the interlaminar stresses of a composite plate around the neighborhood of a hole. International Journal of Solids and Structures 25, 1193–1200.

Iarve, E.V., 1996. Spline variational three-dimensional stress analysis of laminated composite plates with open holes. International Journal of Solids and Structures 44 (14), 2095–2118.

Iarve, E.V., 1997. Three-dimensional stress analysis in laminated composites with fasteners based on the B-spline approximation. Composites Part A 28A, 559–571.

Iarve, E.V., 2000. Asymptotically exact stresses in laminates with rigid fastener. Journal of Composite Science and Technology 60, 2365–2374.

Iarve, E.V., Pagano, N.J., 2001. Singular full-field stresses in composite laminates with open holes. International Journal of Solids and Structures 38 (1), 1–28.

Sihn, S., Iarve, E.V., Roy, A.K., accepted for publication. Three-dimensional stress analysis of textile woven composites: Part I. Numerical analysis. International Journal of Solids and Structures.

Wang, S.S., Choi, I., 1982. Boundary-layer effects in composite laminates: Part 1. Free-edge stress singularities. Journal of Applied Mechanics 49, 541–560.

Wang, S.S., Lu, X., 1993. Three-dimensional asymptotic solutions for interlaminar stresses around cutouts in fiber composite laminates. Mechanics of Thick Composites AMD 1962, 41–50.